4D MAP MRI IMAGE RECONSTRUCTION

Jacob Hinkle[1], Ganesh Adluru[2], Eugene Kholmovski[2], Edward DiBella[2] and Sarang Joshi[1]
[1]*Scientific Computing and Imaging Institute, University of Utah, Salt Lake City, Utah, U.S.A.*
[2]*Utah Center for Advanced Imaging Research, University of Utah, Salt Lake City, Utah, U.S.A.*

Keywords: MRI, Reconstruction, Motion, Diffeomorphic.

Abstract: Conventional MRI reconstruction techniques are susceptible to artifacts when imaging moving organs. In this paper, a reconstruction algorithm is developed that accommodates respiratory motion instead of using only navigator-gated data. The maximum a posteriori (MAP) algorithm uses the raw k-space time-stamped data and the 1D diaphragm navigator signal to reconstruct the images and estimate deformations in anatomy simultaneously. The algorithm eliminates blurring due to binning the data and increases signal-to-noise ratio (SNR) by using all of the collected data. The algorithm is tested in a simulated torso phantom and is shown to increase image quality by dramatically reducing motion artifacts.

1 INTRODUCTION

Conventional MRI reconstruction techniques are susceptible to artifacts when imaging moving organs. Navigators are often used in MRI to handle respiratory motion. The navigator rapidly images a 1D "pencil" perpendicular to the diaphragm. This gives a 1D signal in which the position of the diaphragm in the superior-inferior direction can be found in nearly real-time. In the heart, part of the k-space of the image is acquired following each navigator for a brief period corresponding to cardiac diastole. Diastole is defined by the electrocardiogram (ECG) signal from the subject. This k-space data is marked to be used if the position of the diaphragm is within an acceptance window set by the user. Otherwise, that portion of k-space is re-acquired during the next heartbeat. The navigator is repeated each heartbeat, as is the collection of part of the image k-space, until all of k-space is acquired and marked usable. This respiratory gating algorithm can prolong the acquisition significantly. Increasing the acceptance window shortens acquisition time but leads to image blurring.

In this paper, we take an alternate approach by developing a reconstruction algorithm that accommodates motion instead of discarding k-space data acquired when the diaphragm position is outside the acceptance window. The maximum a posteriori (MAP) algorithm uses raw time-stamped data to reconstruct the images and estimate deformations in anatomy simultaneously. The algorithm eliminates artifacts by avoiding gating processes and increases signal-to-noise ratio (SNR) by using all of the collected data. This framework also facilitates the incorporation of fundamental physical properties such as the conservation of local tissue volume during the estimation of the organ motion.

Previous attempts at reducing motion artifacts do not offer all the advantages of our proposed method, which incorporates a fully diffeomorphic motion model into the reconstruction process. As early as 1991, Song and Leahy (Song and Leahy, 1991) used an incompressible optical flow method for image registration. Rohlfing et al. (Rohlfing et al., 2003) use a spline-based model which penalizes tissue compression to perform incompressible image registration. Saddi et al. (Saddi et al., 2007) study incompressible fluid-based registration. Their approach requires solution of Poisson's equation via a multigrid method at each iteration. Despite these efforts in image registration, the incompressible nature of internal organs has not previously been incorporated into the image reconstruction process.

Here we test the feasibility of the new framework on a phantom generated from 3D late gadolinium enhancement imaging of the left atrium (McGann et al., 2008).

Hinkle J., Adluru G., Kholmovski E., DiBella E. and Joshi S. (2010).
4D MAP MRI IMAGE RECONSTRUCTION.
In *Proceedings of the International Conference on Computer Vision Theory and Applications*, pages 251-257
DOI: 10.5220/0002847102510257

2 4D MAP IMAGE RECONSTRUCTION

In conventional magnetic resonance imaging a pulse sequence is designed in order to sample the Fourier transform (k-space) of a 3D image. After acquiring enough data to fill a Cartesian grid, an image $I(x)$ is reconstructed by performing an inverse Fourier transform on the data. Such a method is justified when imaging a static subject. However, severe artifacts are introduced when the patient's anatomy undergoes deformation during the scan.

Instead of avoiding motion artifacts in order to improve image quality, we seek to understand motion by modeling and estimating a four-dimensional image $I(t,x)$. Our method extends that of Hinkle et al. (Hinkle et al., 2009) thatp operates on real tomographic projection data to complex-valued MRI data. The algorithm is described in detail in the following sections.

2.1 MRI Data Acquisition Model

In MRI data acquisiton, values of the Fourier transform of $I(t,x)$ are sampled directly:

$$\mathcal{F}\{I\}(\omega) = \frac{1}{(2\pi)^{3/2}} \int_\Omega I(x) e^{-i\omega\cdot x} dx,$$

where $\Omega \subset \mathbb{R}^3$ is the image domain. Note that both $I(x)$ and $\mathcal{F}\{I\}(\omega)$ are complex numbers. We model our collected data as a collection of sets of measurements of $\mathcal{F}\{I\}(\omega)$ for different values of ω. These sets consist of samples which were acquired within a very short time of one another so that the anatomy is in the same configuration for all samples from the same set. For example, for a Cartesian sampling scheme in which a single line of k-space is obtained at each echo, a set of data consists of all the sampled k-space values along that line. In general, the set of sampled points may lie along a single line, multiple lines, or on some other curve for more exotic sampling schemes. We will denote the sampled sets of k-space locations as Ω_i and their measured values $d_i(\omega), \omega \in \Omega_i$.

Since actual data is contaminated by noise, we model each data point $d_i(\omega)$ as a sample of a normal distribution with mean $\mathcal{F}\{I(t_i,x)\}(\omega)$ and some variance σ^2. If $I(t,x)$ is the true 4D image, the log-likelihood of observing the data is

$$\mathcal{L}(\{d_i\}|I) = -\frac{1}{2\sigma^2} \sum_{i=1}^{N} \int_{\Omega_i} \|\mathcal{F}\{I(t_i,x)\}(\omega) - d_i(\omega)\|_{\mathbb{C}}^2 d\omega. \quad (1)$$

2.2 Motion Model

Having modeled the data acquisition and noise, we could attempt to estimate a 4D image $I(t,x)$ which maximizes the data log-likelihood. Indeed this is the basis of many static reconstruction algorithms which estimate $I(x)$ in order to best fit the data. However, in our case the additional temporal dimension of our image domain forces us either to collect much more data or to make use of some other information.

We model the 4D image as a single 3D image $I_0 \in L^2(\Omega)$ undergoing a time-indexed deformation $h : [0,T] \times \Omega \to \Omega$. In this formulation $I(t,x)$ is written as $I_0 \circ h(t,x)$. The problem at hand is then to estimate both the base image and motion which best fit the data.

The estimated time-indexed deformation is meant to model the motion of real tissue. It is useful to introduce a prior on the motion estimates in order to estimate deformations that are consistent with real tissue and organ properties. One possibility is to model the time-indexed deformation as a fluid flow. The deformation is then fully determined by a set of velocity fields $v(t,x)$, which are defined as

$$v(t,x) = \frac{d}{dt} h(t,x).$$

Note that given this set of velocity fields the deformation can be recovered by integration:

$$h(t,x) = x + \int_0^t v(\tau, h(\tau,x)) d\tau$$

If the velocity fields are all smooth spatially then the resulting integral field is guaranteed to be a diffeomorphism. As organs are not expected to tear apart or drastically change geometry during physiological motion, this is a reasonable requirement for many 4D imaging applications. In order to enforce this property, a formal prior is placed on the velocity fields in the form of an inner product norm,

$$\|v\|_V^2 = \langle v, v \rangle_V = \int_0^T \int_\Omega \|Lv(t,x)\|_{\mathbb{R}^3}^2 dx dt,$$

where L is a differential operator chosen to reflect physical tissue properties. In our implementation, L is defined by $Lv = -\alpha\nabla^2 v - \beta\nabla\nabla\cdot v + \gamma v$ for scalar parameters α, β, and γ. Although in this work we have used a homogeneous operator, L could be spatially-varying reflecting the different material properties of the underlying anatomy.

As discussed, the problem is ill-posed if we do not have an abundance of data. In such a case we need to make further assumptions. Many 4D scanning protocols make use of a navigator echo as a signal indicating respiratory motion. If the signal is

well-correlated with the internal anatomical configuration, it may be used to reduce the data requirements for the 4D reconstruction problem. If a signal, $a(t)$, is a faithful surrogate of the internal anatomy, then $a(t_1) = a(t_2)$ implies that $I(t_1,x) = I(t_2,x)$. This is satisfied if $h(t_1,x) = h(t_2,x)$ for all x. This will be true for all times with matching surrogate signal amplitudes, so it is convenient to index the deformations by amplitude instead of time. Formally, we will write

$$h(t,x) = h(a(t),x).$$

Returning to the definition of $v(t,x)$ the change of variables looks like

$$v(t,x) = \frac{d}{dt}h(a(t),x) = v(a(t),h(a(t),x))\frac{da}{dt},$$

where $v(a,x)$ is a velocity field with respect to changes in surrogate signal instead of time. The deformation to any amplitude is then obtained by the integration of Eq. 2.2,

$$h(a,x) = x + \int_0^a v(a',h(a',x))da'.$$

The motion prior is modified accordingly by replacing the time-indexed velocities with these amplitude-dependent ones:

$$\|v\|_V^2 = \langle v,v\rangle_V = \int_0^1 \int_\Omega \|Lv(a,x)\|_{\mathbb{R}^3}^2 dxda.$$

When modeling organs such as liver which are essentially incompressible during normal activity, unrealistic deformations may be easily recognized if they represent local compression or expansion. Estimation of these types of unrealistic deformations may be avoided by constraining the deformations to be incompressible. Deformations defined as a flow along smoothly-varying vector fields as described in Eq. 2.2 have been well studied (Arnold, 1997). In particular, if the divergence of the velocity field is zero the resulting deformation is guaranteed to preserve volume locally and have unit Jacobian determinant. It will be useful to enforce this constraint in our algorithm when modelling incompressible tissue.

2.3 Posterior Likelihood and Optimization

The data log-likelihood and motion prior are combined to give the posterior log-likelihood,

$$\mathcal{L}(I_0,v|d_i) = -\|v\|_V^2 - \frac{1}{2\sigma^2}\sum_{i=1}^N \int_{\Omega_i} \|\mathcal{F}\{I_0 \circ h(a_i,\cdot)\}(\omega) - d_i(\omega)\|_{\mathbb{C}}^2 d\omega. \tag{2}$$

The 4D image reconstruction problem is to estimate the image and velocity fields that maximize Eq. 2,

$$(\hat{I}_0,\hat{v}) = \underset{I_0,v}{\operatorname{argmax}}\, \mathcal{L}(I_0,v|d_i) \qquad \text{subject to } \operatorname{div} v = 0.$$

A MAP estimate (one that maximizes Eq. 2) is obtained via an alternating iterative algorithm which at each iteration updates the estimate of the deformation in a gradient ascent step then updates the image.

The continuous amplitude-indexed velocity field is discretized by a set of equally-spaced amplitudes a_k with the associated velocities v_k, with spacing Δa. Note that this amplitude discretization is independent of the amplitudes at which data is acquired. The deformation from amplitude a_k to a_{k+1} is approximated by the Euler integration of Eq. 2.2,

$$h(a_{k+1},x) = h(a_k,x) + v_k(h(a_k,x))$$

and the deformation for an amplitude a_i between a_k and a_{k+1} is linearly interpolated as

$$h(a_i,x) = h(a_k,x) + \frac{a_i - a_k}{\Delta a} v_k(h(a_k,x)).$$

Note that higher order integration schemes such as Runge-Kutta may also be used in place of the simpler Euler method.

The first variation of Eq. 2 with respect to v_k under the inner product in Eq. 2.2 is given by

$$\delta_{v_k}\mathcal{L}(I_0,v_k,x|d_i) = -2v_k(x) - \frac{1}{\sigma^2}(L^\dagger L)^{-1}\sum_{i=1}^N \operatorname{Re}\left[g_i(x)b_i(k,x)^*\right], \tag{3}$$

where $g_i(x) = \mathcal{F}^{-1}\left(\mathcal{F}\{I_0 \circ h(a_i,\cdot)\} - d_i\right)(x)$ and b_i is the contribution to the variation due to data set i, defined as follows.

Let $I_k(x) = I_0 \circ h(a_k,x)$ be the 3D reference image pushed forward to amplitude a_k. Then the factors b_i are given by

$$b_i(k,x) = \begin{cases} 0 & a_i \le a_k \\ \frac{a_i-a_k}{\Delta a}\nabla I_k(x + \frac{a_i-a_k}{\Delta a}v_k(x)) & a_k < a_i \le a_{k+1} \\ J_{i,k+1}\nabla I_k(x+v_k(x)) & a_i > a_{k+1}, \end{cases}$$

where $J_{i,k+1}$ is the Jacobian determinant of the transformation from amplitude a_i to a_{k+1}, $\left|D(h_{a_{k+1}} \circ h_{a_i}^{-1})(x)\right|$. If the deformations are constrained to be incompressible, implying that the Jacobian determinant is unity, this simplifies to

$$b_i(k,x) = \begin{cases} 0 & a_i \le a_k \\ \frac{a_i-a_k}{\Delta a}\nabla I_k(x + \frac{a_i-a_k}{\Delta a}v_k(x)) & a_k < a_i \le a_{k+1} \\ \nabla I_k(x+v_k(x)) & a_i > a_{k+1}. \end{cases}$$

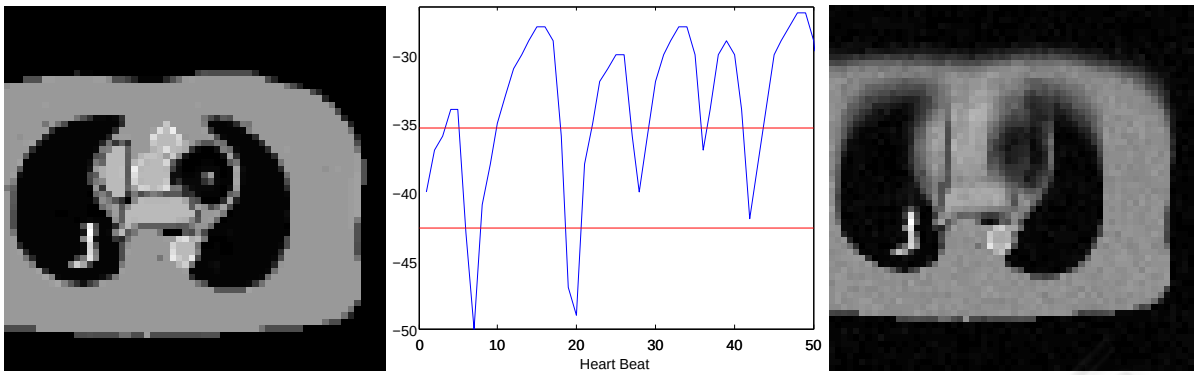

Figure 1: Static phantom (left), breathing signal from real patient navigator echo used in simulation with red lines indicating boundary between bins used in binning method (center), and static 3D reconstruction of data from moving phantom (right).

Following the approach of Beg et al. (Beg et al., 2005), efficient computation of $(L^\dagger L)^{-1}$ is implemented in the Fourier domain, requiring only a matrix multiplication and Fourier transforms of v_k at each iteration of the algorithm.

The first variation of Eq. 2 with respect to I_0 is

$$\delta_{I_0}\mathcal{L}(I_0,v,x|d_i) = \frac{1}{\sigma^2}\sum_i |Dh^{-1}(a_i,x)|g_i(x)\circ h^{-1}(a_i,x). \tag{4}$$

With these variations a gradient descent algorithm can be implemented. However, as discussed previously, it is sometimes useful to enforce further tissue constraints. The Helmholtz-Hodge decomposition allows us to implement the incompressibility constraint by simply projecting the unconstrained velocity fields onto the space of divergence-free vector fields at each iteration of the algorithm (Cantarella et al., 2002). In order to efficiently implement the Helmholtz-Hodge decomposition of a time-varying velocity field, we use the discrete divergence operator as it operates in Fourier domain. We write the discrete Fourier transform of a central difference approximation to the derivative of a function f as

$$\mathrm{DFT}\{\Delta_x f\}(\omega) = \frac{i}{2k_x}\sin\omega\,\mathrm{DFT}\{f\}(\omega).$$

In the Fourier domain the divergence of a vector field takes the following form:

$$\mathrm{DFT}\{\mathrm{div}\,v\}\ (\omega) = W(\omega)\cdot\mathrm{DFT}\{v\}(\omega),$$

where

$$W(\omega) = \frac{i}{2}\begin{pmatrix} \frac{1}{k_x}\sin\frac{\omega_x}{N_x} \\ \frac{1}{k_y}\sin\frac{\omega_y}{N_y} \\ \frac{1}{k_z}\sin\frac{\omega_z}{N_z}\end{pmatrix}.$$

This allows us to remove the divergent component easily in Fourier space via the projection

$$\mathrm{DFT}\{v\}(\omega) \mapsto \mathrm{DFT}\{v\}(\omega) - \frac{W(\omega)\cdot\mathrm{DFT}\{v\}(\omega)}{\|W(\omega)\|^2_{\mathbb{C}^3}}W(\omega). \tag{5}$$

$I_0 \leftarrow 0$
for each k **do**
  $v_k \leftarrow 0$
end for
repeat
  $I_0 \leftarrow I_0 + \varepsilon\delta_{I_0}\mathcal{L}(I_0,v)$
  for each k **do**
    $v_k \leftarrow v_k + \varepsilon\delta_{v_k}\mathcal{L}(I_0,v_k)$
    $v_k \leftarrow$ Perform divergence-free projection on v_k (optional)
  end for
until algorithm converges or maximum number iterations reached

Figure 2: Pseudocode for 4D reconstruction.

Since the operator $(L^\dagger L)^{-1}$ is implemented in the Fourier domain there is little computational overhead in performing this projection at each iteration of the algorithm.

Note that as soon as the velocity field is updated, the image estimate must also be updated. The change of image estimate in turn alters the velocity gradients leading to a joint estimation algorithm in which, at each iteration, the velocity fields are updated and then the image recalculated.

Figure 2 summarizes the 4D reconstruction procedure. The velocity fields are initialized to zero, so that the initial estimate of the base image is simply the result of averaging all of the data. This yields a quite blurry image that sharpens upon further iterations as the motion estimate improves.

3 RESULTS

A realistic 3D phantom was created from a late gadolinium enhancement (LGE) acquisition of a post-ablation patient (Peters et al., 2007; McGann et al., 2008) acquired on a Siemens Verio 3T scanner. Reso-

lution was 1.25x1.25x2.5mm and 40 slices were acquired. 19 different structures were manually segmented and assigned different T1 values. The inversion time was chosen to null myocardial signal. A single slice was extracted to test the MAP image reconstruction method. This slice was downsampled to 60x60 pixels and k-space measurements of the slice were simulated as 30 phase encodes per heartbeat. Each set of 30 phase encodes was subjected to a deformation. The deformation was designed to simulate the motion of the torso during breathing. The spine and back stayed stationary while the chest wall and anterior portion of the torso moved in the anterior direction. The motion was designed to be proportional to a breathing signal $a(t)$ which was extracted from a navigator echo of the patient. Both the 2D phantom and the respiratory signal used to generate the deformations are shown in Fig. 1.

A static reconstruction of the simulated data was performed by averaging the recorded values at each point in k-space then performing an inverse discrete Fourier transform on the resulting 2D grid. Figure 1 shows the resulting image. Notice the extreme blurring artifacts caused by averaging all of the collected data while ignoring motion.

The breathing signal was then used to bin the simulated k-space data into three bins. The boundaries between bins are displayed as red lines in Fig. 1. Note that the bottom bin has very few data points. The result is that this bin cannot be reliably reconstructed. This illustrates a major difficulty associated with binning or gating. The comparisons that follow will deal only with the top two bins, in which there is enough data that the binning method might have a realistic chance of producing an image.

A 4D MAP reconstruction was also performed on the same data. The static phantom, static reconstruction of moving phantom, and 4D MAP reconstruction of moving phantom are shown in Fig. 4. Notice the improvement in image quality. In particular, the 4D MAP reconstruction avoids the blurring of edges seen in the static reconstruction. Also note the decreased noise in the 4D MAP reconstructed images as compared to the binned images. This illustrates the advantages of techniques which use all of the data, such as 4D MAP reconstruction, as opposed to gating or binning. For comparison purposes, only two images are shown of the 4D MAP reconstruction. However, images can easily be generated corresponding to any breathing amplitude. This contrasts gating and binning procedures, in which more data needs to be acquired in order to generate more images.

Figure 3 shows a plot of the objective function, Eq. 2, as the algorithm ran. Note that the shape of the plot indicates that the algorithm has converged. This algorithm employs a gradient descent method, as discussed previously. However, many optimization schemes exist which could replace this simple method and possibly offer faster convergence.

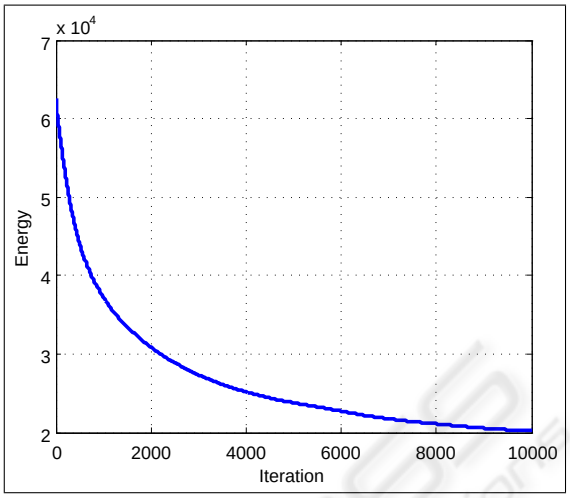

Figure 3: Convergence plot showing that the posterior likelihood has been minimized.

In addition to improving the image estimates, a valuable motion estimate is also obtained during 4D reconstruction. Figure 5 shows a comparison of the true deformation applied to the phantom in order to generate the data and that obtained by the 4D MAP reconstruction algorithm. Note that the fully high-dimensional deformation has been estimated quite accurately. The algorithm is of course not able to reliably estimate motion in areas where the image is homogeneous, as indicated by the slight deviations near the right and left edges of the image.

4 CONCLUSIONS

A 4D reconstruction method was shown to reduce motion artifacts in simulation. Instead of avoiding motion effects by discarding data acquired when the diaphragm was not within an acceptance window, the method estimates the motion directly from all of the raw data. The method was shown to reduce blurring artifacts in a two-dimensional phantom. In addition, SNR was improved. These are critically important considerations for many respiratory-gated MRI studies. Not only were the images improved but a valuable motion estimate was obtained. This motion estimate was shown to be accurate in regions where the anatomy has sufficient contrast to enable tracking of tissue.

The results in this paper were implemented in

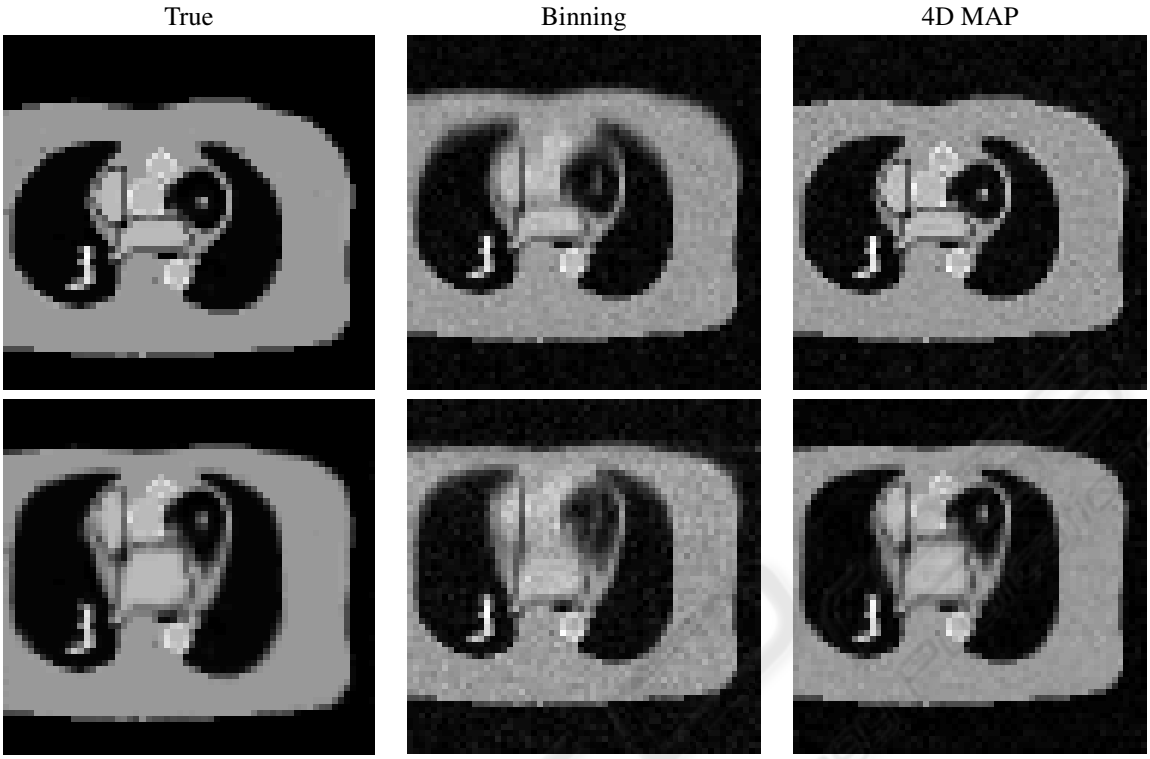

Figure 4: True phantom along with binned and 4D MAP reconstructed images. The top row shows reconstructions at amplitude $a = 1$, while the bottom row shows reconstructions at amplitude $a = 0.5$.

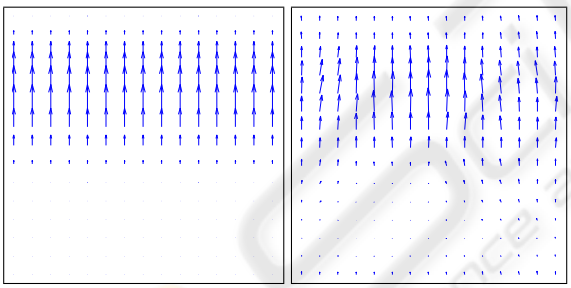

Figure 5: The true velocity field used to generate simulated data (left) and the motion estimate resulting from 4D MAP reconstruction (right).

MATLAB using a 2D version of the algorithm. The method will be extended to real 4D data from MRI of patients being treated for atrial fibrillation. Current efficiencies of the respiratory navigator scan range from 20% to 60%, implying the methods here could substantially improve the image quality and/or allow for a more rapid scan by using a larger acceptance window.

The move to true 4D reconstruction is conceptually trivial, but will introduce added computation, as the amount of lines will increase as well as the size of the estimated images and velocity fields. However, the algorithm lends itself particularly well to parallel computation which should allow even the full 3D implementation to run in a reasonable amount of time.

The intent of this work is to introduce a framework by which 4D data was reconstructed using a motion surrogate signal. The framework is flexible and could be extended for other applications. The motion signal was extracted from a navigator echo sequence, giving a direct measure of internal anatomy. However, if a navigator echo is unsuitable for a particular scan, another respiratory signal could be used, such as a chest marker or spirometer. Also, if enough data is available the motion surrogate could be ignored and time-indexed deformations estimated.

There are other possible extensions to the algorithm presented in this paper. For instance, if an artifact-free base image is available, this can be directly used to obtain a best fit deformation estimate. The reconstruction algorithm also does not dictate what k-space trajectory to use. A Cartesian sampling scheme was simulated in this work but other trajectories such as spiral and polar acquisitions could be used with very little modification to the algorithm.

REFERENCES

Arnold, V. I. (1997). *Mathematical Methods of Classical Mechanics*. Springer, 2nd edition.

Beg, M. F., Miller, M. I., Trouvé, A., and Younes, L. (2005). Computing large deformation metric mappings via geodesic flows of diffeomorphisms. *Int. J. Comp. Vis.*, 61(2):139–157.

Cantarella, J., DeTurck, D., and Gluck, H. (2002). Vector calculus and the topology of domains in 3-space. *Amer. Math. Monthly*, 109(5):409–442.

Hinkle, J., Fletcher, P. T., Wang, B., Salter, B., and Joshi, S. (2009). 4D MAP image reconstruction incorporating organ motion. In *IPMI 2009: Proceedings of Information Processing in Medical Imaging*, pages 676–687.

McGann, C. J., Kholmovski, E. G., Oakes, R. S., Blauer, J. J., Daccarett, M., Segerson, N., Airey, K. J., Akoum, N., Fish, E., Badger, T. J., DiBella, E. V., Parker, D., MacLeod, R. S., and Marrouche, N. F. (2008). New magnetic resonance imaging-based method for defining the extent of left atrial wall injury after the ablation of atrial fibrillation. *J Am Coll Cardiol*, 52:1263–1271.

Peters, D. C., Wylie, J. V., Hauser, T. H., Kissinger, K. V., Botnar, R. M., Essebag, V., Josephson, M. E., and Manning, W. J. (2007). Detection of pulmonary vein and left atrial scar after catheter ablation with three-dimensional navigator-gated delayed enhancement MR imaging: Initial experience. *Radiology*, 243:690–695.

Rohlfing, T., Calvin R. Maurer, J., Bluemke, D. A., and Jacobs, M. A. (2003). Volume-preserving nonrigid registration of MR breast images using free-form deformation with an incompressibility constraint. *IEEE Trans. Med. Imag.*, 22(6):730–741.

Saddi, K. A., Chefd'hotel, C., and Cheriet, F. (2007). Large deformation registration of contrast-enhanced images with volume-preserving constraint. In *Proceedings of International Society for Optical Engineering (SPIE) Conference on Medical Imaging 2007*, volume 6512.

Song, S. M. and Leahy, R. M. (1991). Computation of 3-D velocity fields from 3-D cine CT images of a human heart. *IEEE Trans. Med. Imag.*, 10(3):295–306.